Journal of ELECTRONIC MATERIALS, Vol. 38, No. 12, 2009
DOI: 10.1007/s11664-009-0889-x

Mechanical Shock Behavior of Bulk Pure Sn Solder

K.E. YAZZIE,[1] H. FEI,[2] J.J. WILLIAMS,[1] H. JIANG,[2] and N. CHAWLA[1,2,3]

1.—School of Materials, Arizona State University, Tempe, AZ 85287-8706, USA. 2.—Department of Mechanical and Aerospace Engineering, Fulton School of Engineering, Arizona State University, Tempe, AZ 85287-8706, USA. 3.—e-mail: nchawla@asu.edu

With the increasing focus on developing environmentally benign electronic packages, Pb-free alloys have received a great deal of attention. Mishandling of packages during manufacture, assembly or by the user may cause failure of the solder joint. A fundamental understanding of the behavior of Pb-free solders under mechanical shock conditions is lacking. Reliable experimental stress–strain data over a range of strain rates needs to be obtained for reliability models. In this paper we report on the intermediate strain rate behavior of pure Sn solder. The first part of the paper discusses modeling and analysis of the specimen geometry to obtain a relatively uniform stress (and strain) distribution within the gage section. Analysis by the finite element method (FEM) showed that a modified specimen geometry, with 10 mm gage length, provided a homogeneous strain distribution, similar to the American Society for Testing and Materials (ASTM) E8 specimen geometry. The second part describes microstructural characterization and experimental results on pure Sn at intermediate strain rates (~10/s). Ultimate tensile strength and strain to failure in the 10 mm specimen were quite similar to those of the ASTM specimen. A double necking phenomenon was observed in the ASTM specimen, which was not observed in the 10 mm specimen. FEM modeling of the dynamic behavior of the solder correlated very well with the experimental observations.

Key words: Pb-free solder, mechanical shock, high-speed video, necking

INTRODUCTION

With the increasing focus on developing environmentally benign electronic packages, Pb-free alloys have received a great deal of attention.[1–7] Mishandling of packages during manufacture, assembly or by the user may cause failure of the solder joint. While we now have a good understanding of microstructure, creep, and thermal fatigue behavior of Pb-free solders,[8–11] other important issues related to deformation in these materials remain to be addressed. In particular, a fundamental understanding of the behavior of Pb-free solders under mechanical shock conditions is lacking. Reliable experimental stress–strain data over a range of strain rates needs to be obtained for reliability models.

(Received March 21, 2009; accepted June 20, 2009; published online July 28, 2009)

A variety of experimental techniques have been developed to characterize the strain–rate-dependent behavior of materials.[12] Conventional screw-driven machines can be used to quantify creep and stress relaxation processes at very slow strain rates. At the high end, or impact regime, plate impact is typically used. The strain rates obtained during mechanical shock of solders, such as that experienced by dropping a cellphone or laptop, is somewhere between the quasistatic and dynamic strain range. In fact, a precise value or range of strain rate for these applications has not yet been established. The range from a variety of studies is somewhere between 10^{-1}/s and 10^{2}/s.[13–19] A promising technique that has yet to be applied to dynamic testing of solders is impact using servohydraulic methods. Boyce and Crenshaw[20] have demonstrated that controlled strain rates of up to 500/s (much higher than that required for solder materials) can be obtained on relatively small specimens using modified

servohydraulic methods. Thus, this is a highly desirable technique needed to characterize the mechanical shock of solders in the intermediate strain rate regime.

In this paper we report on the intermediate strain rate behavior of pure Sn solder. The first part of the paper discusses modeling and analysis of the specimen geometry to obtain a relatively uniform stress (and strain) distribution within the gage section. The second part describes microstructural characterization and experimental results on pure Sn at intermediate strain rates (~10/s). This is followed by a presentation of numerical simulation of deformation in the solder.

MATERIALS AND EXPERIMENTAL PROCEDURE

High-purity cast ingots of Sn (Indium Corporation, Ithaca, NY, USA, and Alfa Aesar, Ward Hill, MA, USA) were used in this study. The ingots were reflowed in an aluminum mold coated with graphite to yield rectangular blanks approximately 10.5 cm in length, 1 cm in width, and 0.8 cm in height. A thermocouple was placed at the bottom of the solder to determine the cooling rate in the solder. Samples were heated at 250°C (approximately 20°C above the melting point of the solder) for 20 s and furnace-cooled, yielding a reproducible cooling rate of about 0.1°C/s. Microstructural characterization was conducted after reflow and cooling. Samples were polished to a final finish with a 0.05 μm colloidal silica solution. Optical microscopy was carried out in order to quantify the microstructure. Tensile specimens were machined from a section near the bottom of the reflowed blank, where the cooling rate was measured. Microstructure characterization of the tensile specimens prior to testing indicated a uniform microstructure throughout the samples.

Finite element method (FEM) was used to determine an appropriate specimen geometry for testing. Smaller gage sections allow for a higher strain rate, but potentially nonuniform strain in the gage volume. Thus, three specimen geometries were considered in finite element modeling: the ASTM E-8M standard geometry with a gage length of 25 mm as shown in Fig. 1a, a smaller geometry with a gage length of 10 mm as shown in Fig. 1b, and an even smaller geometry with a gage length of 5 mm as shown in Fig. 1c. The overall length of the ASTM E-8M specimen was 100 mm, while the overall length of the 10 mm and 5 mm gage length specimens was close to 50 mm. All three specimens had a thickness of 6 mm, a width of 4 mm in the gage length, a width of 10 mm in the grip sections, and a fillet radius of 6 mm. Based on the modeling results presented in the "Results and Discussion" section, only the ASTM E-8M geometry and the 10 mm gage length specimens were used for tensile testing. Tensile tests were performed on a servohydraulic load frame, in displacement control, to achieve a nominal strain rate of 10/s.

A high-speed camera (Phantom, Vision Research, Wayne, NJ) with an acquisition rate of 2100 frames per second (at its highest resolution), was used to measure strain on the solder specimen. Strain was calculated in two ways: (a) macroscopic strain given using an extensometer with 25 mm gage length and (b) by local strain measurement using digital images of fiducial lines on the specimen surface. Figure 2a shows the experimental setup of the servohydraulic load frame, high-speed camera, and video processing station. Figure 2b shows how fiducial lines were used in combination with an extensometer to calibrate the displacement rate using ASTM E-8M specimens. The size constraint of the extensometer precluded its use with the 10 mm specimens. Fiducial lines were marked on the

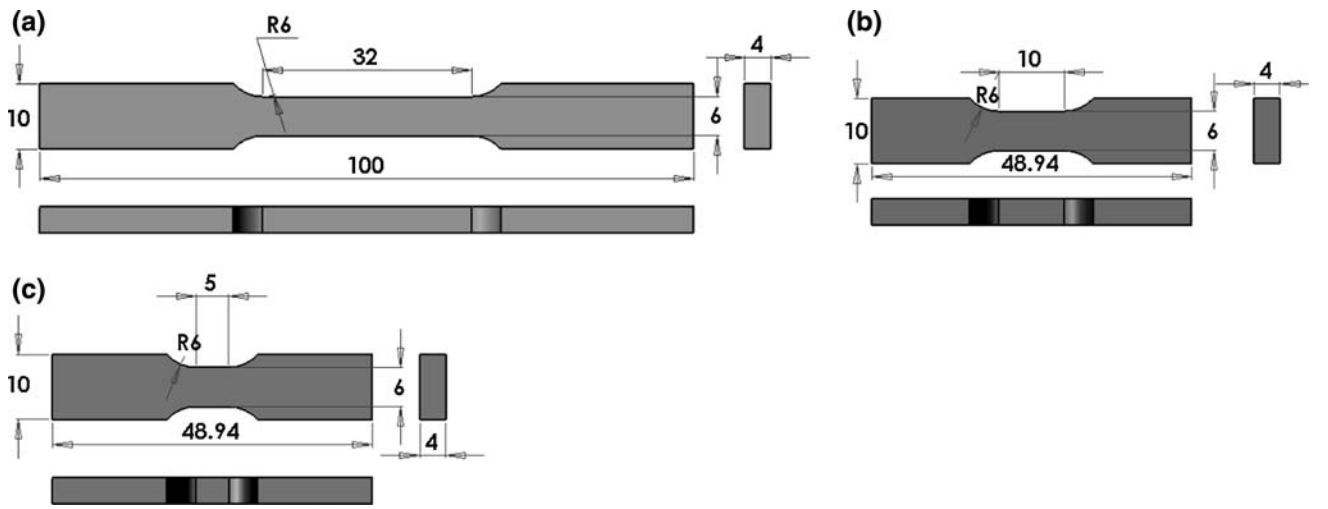

Fig. 1. Specimen geometries studied using finite element modeling: (a) ASTM E8 specimen geometry with a gage length of 25 mm, and a total reduced section of 32 mm, (b) specimen geometry with 10 mm gage length, and (c) specimen geometry with 5 mm gage length. All dimensions are in mm.

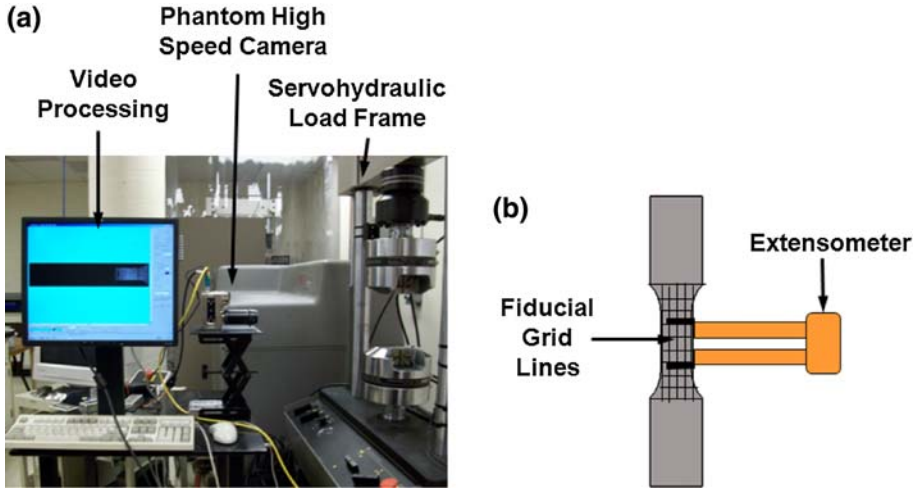

Fig. 2. (a) Setup for high-speed camera system and servohydraulic load frame. (b) Strain measurement methods used: displacement of fiducial lines and extensometer; the fiducial lines had a longitudinal spacing of 2.5 ± 0.1 mm and a transverse spacing of 1.5 ± 0.1 mm.

specimen surface, using a razor blade, forming a rectangular grid with a longitudinal spacing of 2.5 ± 0.1 mm and a transverse spacing of 1.5 ± 0.1 mm.

RESULTS AND DISCUSSION

Microstructure characterization of the reflowed and machined pure Sn bars showed a fairly uniform grain structure, although some elongation of the grains was observed (Fig. 3). Table I presents results of the grain size measurements, based on the linear intercept technique. Here, a grid is overlaid over the microstructure and the number of intercepts is used to calculate an average grain size. The grain size along the length of the specimen was about half that along the width of the specimen. A statistically representative number of grains was present in the gage section of the specimens. The microstructure of the specimens was also compared before and after machining, and did not show any statistical difference.

Intermediate strain rate experiments in solders can be conducted in strain control or displacement control. Initial experiments conducted in strain control yielded a "lag" in the desired strain rate response. In other words, the machine was not able to respond quickly enough to achieve the desired strain rate. Thus, it was decided to conduct the experiments in displacement control. The strain rate, $\dot{\varepsilon}$, is related to the applied displacement, ΔL, as follows:

$$\dot{\varepsilon} = \frac{\varepsilon}{t} = \frac{\Delta L}{L} \cdot \frac{1}{t},$$

where L is the gage length of the specimen and t is time. The maximum displacement rate, $\Delta L/t$, is a function of the flow rate in the servohydraulic machine, the mass of the grips, etc. In our case,

Table I. Grain Size of Pure Sn Solder

Orientation	Number of Intercepts	Average Grain Size (μm)
Longitudinal	203	36.5 ± 6.6
Transverse	107	72.5 ± 26.4

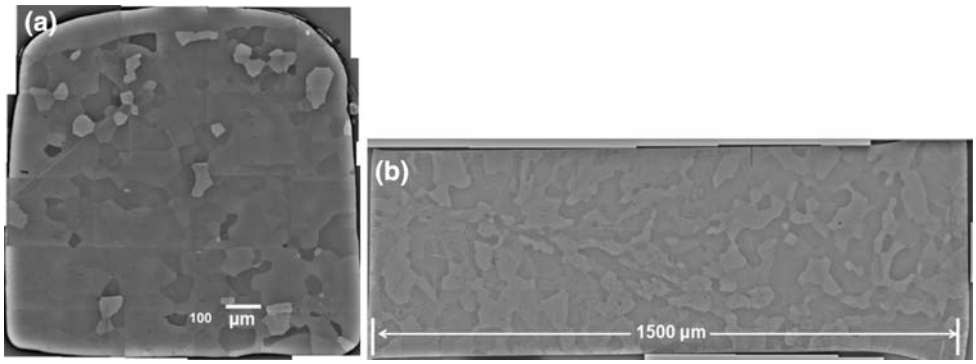

Fig. 3. Microstructure of reflowed and machined pure Sn bars: (a) transverse microstructure and (b) longitudinal microstructure.

the maximum displacement rate possible was about 300 mm/s. The other way to increase the strain rate is to decrease the gage length, L. It should be noted that this must be done carefully because decreasing the gage length too much may yield a nonuniform stress distribution in the gage volume. In order to quantify this effect, we conducted a simple finite element analysis to determine the change in stress and strain state when going from the ASTM E-8M gage length (25 mm), to 10 mm, and 5 mm. This was followed by experimental characterization at a strain rate of about 10/s and modeling of the effect of strain rate.

As mentioned above, the ASTM E-8M, 10 mm gage length, and 5 mm gage length specimen geometries were modeled in order to quantify stress heterogeneity as a function of gage length. True stress and true strain data from a tensile test of an ASTM E-8M specimen of furnace-cooled pure Sn, conducted at a strain rate of 0.2/s, was used as the constitutive response of the material. The true stress and true strain input is shown in Fig. 4a. The effect of strain rate was not included here, since these models were only used to quantify stress and strain heterogeneity in the gage section of the specimen. Only the gage section and fillet regions were modeled because in a tensile test the grip sections would be clamped, resulting in essentially fixed boundary conditions (U2 = U3 = 0) at the fillet sections. Figure 4b shows the gage section and fillet regions modeled, and the boundary conditions. A mesh of quadratic hexahedral elements was used. A mesh refinement study using the ASTM E-8M model was conducted by incrementally increasing the mesh density. All specimens were displaced to produce an equivalent strain of 0.02 in their respective gage sections. The average stress and standard deviation in the elements, measured over

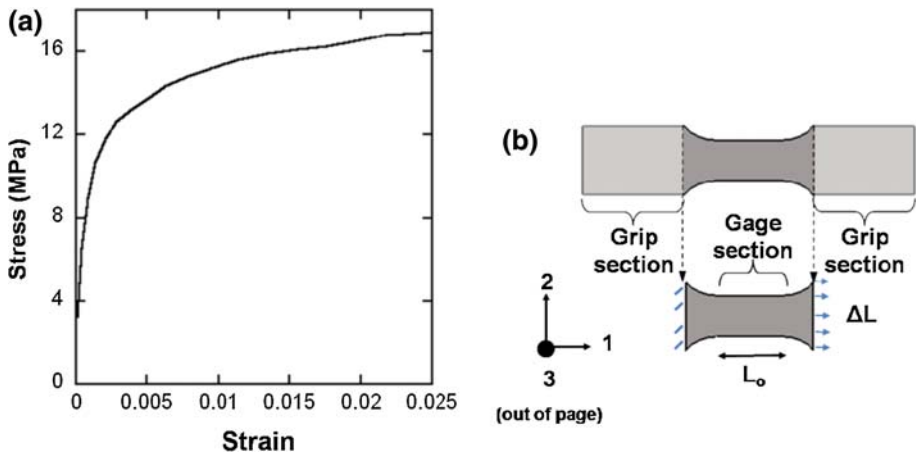

Fig. 4. Parameters used to model the stress heterogeneity as a function of gage length. (a) Constitutive material response obtained from a tensile test of an ASTM E8 specimen of furnace-cooled pure Sn, conducted at a strain rate of 0.2/s. (b) Boundary conditions applied to a model of the gage section and fillet regions.

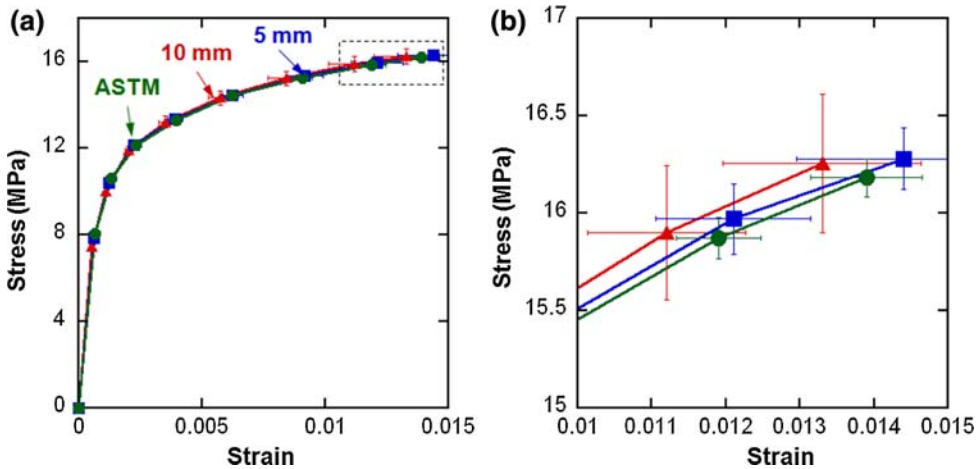

Fig. 5. Comparison of stress–strain behavior, obtained from finite element analysis, for the different gage sections. (a) Average stress–strain and standard deviations measured over the elements in the gage section. (b) Magnified region close to the ultimate tensile strength showing that the 10 mm gage length model more closely approximates the stress–strain behavior of the ASTM E8 model.

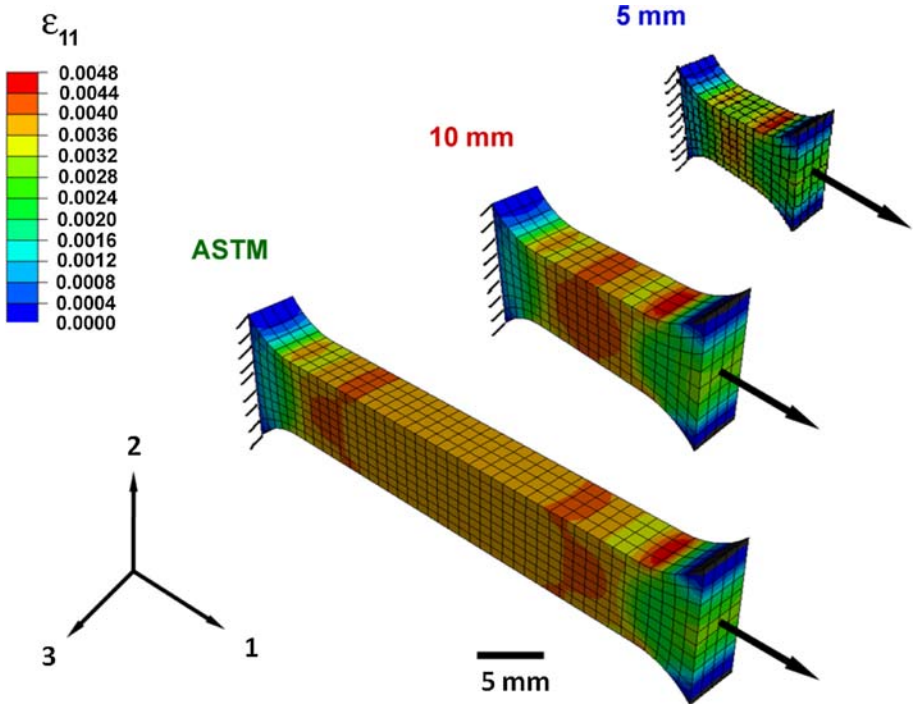

Fig. 6. Axial strain (ε_{11}) contours for all three models. The 5 mm gage length model has the most heterogeneous strain distribution in the gage section. The 10 mm gage length model has a reasonably wide region of uniform strain and similar stress–strain behavior to the ASTM-E8 model.

Table II. Summary of Tensile Results for ASTM and 10 mm Gage Length Specimen Geometry

Specimen Geometry	Ultimate Tensile Strength (MPa)	Strain-to-Failure	Strain Rate (/s)
ASTM E8 (24 mm gage length)	42.3 ± 7.2	0.93 ± 0.09	9.8 ± 0.4
10 mm gage length	44.5 ± 7.4	1.08 ± 0.18	9.9 ± 0.1

the gage sections of the models, are plotted versus applied strain in Fig. 5a. Figure 5b shows that the 5 mm gage length model deviates most from the ASTM E-8M model and has the largest standard deviation in stress and strain. The 10 mm gage length specimen more closely approximates the stress–strain behavior of the ASTM E-8M model. Figure 6 shows the axial strain (ε_{11}) contours for all three models. The 5 mm gage length model has the most heterogeneous strain distribution in the gage section, whereas the 10 mm gage length model has a reasonably wide region of uniform strain. The ASTM E-8M model has uniform strain throughout the entire 25 mm gage section. Based on this analysis, the ASTM E-8M and 10 mm gage length geometry were used for the tensile tests reported herein.

Table II presents a summary of the ultimate tensile strength (UTS), strain-to-failure, and testing strain rate. The strain rate was about 10/s for both specimen geometries. Note that σ_{UTS} and strain-to-failure were also very similar, indicating that the 10 mm geometry is suitable for tensile testing, in

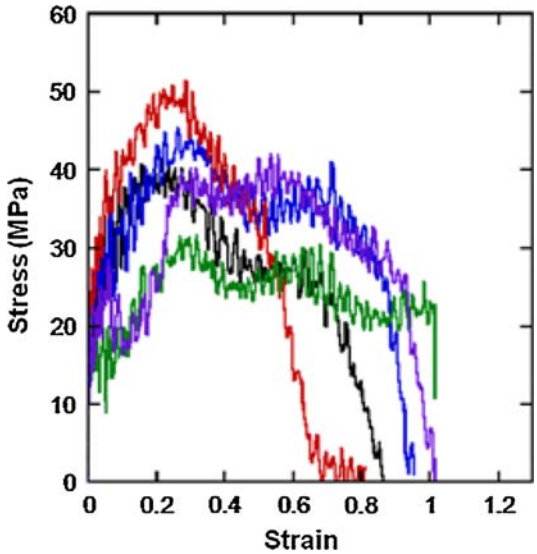

Fig. 7. Stress–strain curves for tensile tests conducted at a strain rate of 10/s using ASTM E8 specimens. Several curves exhibit two distinct "peaks" due to double necking. Oscillations in the stress–strain curve are due to reflected elastic waves.

this strain rate regime. Examination of the stress–strain curves, for both geometries, showed that while σ_{UTS} and strain-to-failure were indeed similar, the curves for the 25 mm gage section exhibited two distinct "peaks" in the stress–strain curve (Fig. 7). Using the high-speed video, it was noted that the peaks corresponded to two separate necks forming in the gage section (Fig. 8). The phenomenon of multiple necking at high strain rates has been observed in other materials, such as aluminum and copper.[21–23] The dynamics of plastic instability are quite complicated and are not treated here. The smaller gage section, on the other hand, only exhibited one peak in the curve. Within the population of these curves, two experiments had somewhat higher ultimate tensile strength and lower ductility (Fig. 9a). Videos of these experiments indicated a fair amount of bulging in the gage section, due to some degree of inhomogeneous deformation (Fig. 9b). The reasons for bulging in some specimens are likely related to the evolution of deformation, perhaps due to individual grain orientation and/or defects. A more detailed study is needed to understand this behavior.

We now present the simulation of deformation at various strain rates. The objective of the theoretical study is to qualitatively explain the experimentally observed behavior, as influenced by gage length and applied strain rate. This analysis was conducted using ABAQUS/Explicit.[24] To accurately investigate the geometric effects on the double necking, we used three-dimensional elements. In order to ensure convergence of the explicit analysis, a very fine mesh and time increment were used. After the studies of mesh sensitivity, element C3D8R (continuum three-dimensional eight-node solid element with reduced integration scheme) was chosen. Depending on the geometry of our model system, the total number of elements ranged from 6000 to 27,820.

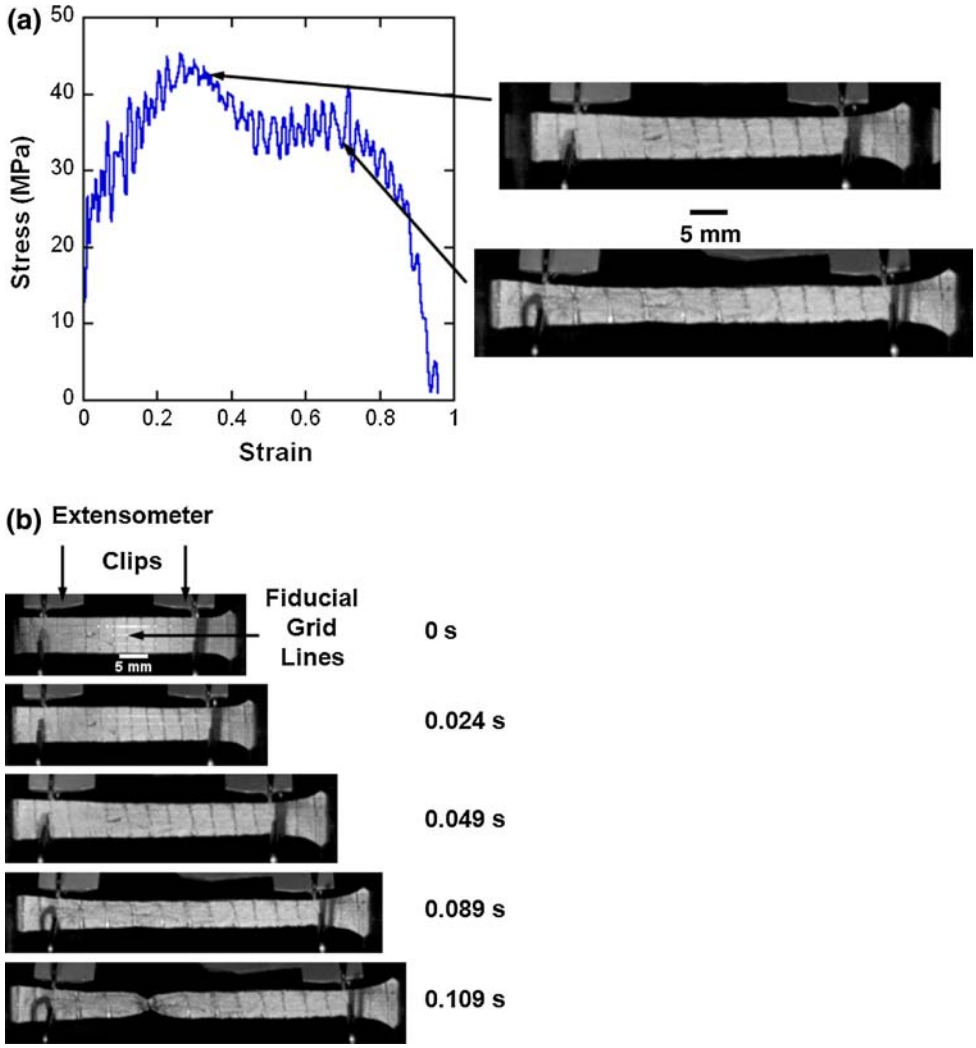

Fig. 8. High-speed video analysis of ASTM E8 specimen tensile tests. (a) High-speed video shows that the "peaks" correspond to formation of two time-separated necks in the gage section. (b) Still images from selected points in the entire test sequence showing the progression of specimen deformation.

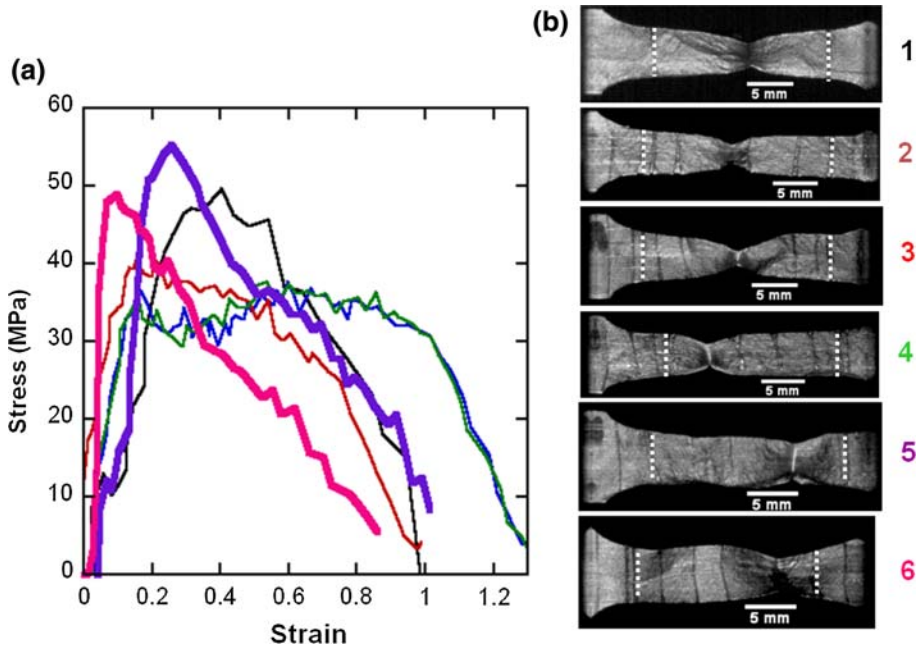

Fig. 9. (a) Stress–strain curves of 10 mm gage length specimens tested at a strain rate of 10/s. Two experiments, which had somewhat higher σ_{UTS} and strain-to-failure, are indicated by bold line thicknesses. (b) High-speed video analysis of the experiments indicated bulging in some specimens; especially for specimens 5 and 6 which correspond to the bold curves in (a). Gage sections are indicated by white dotted lines.

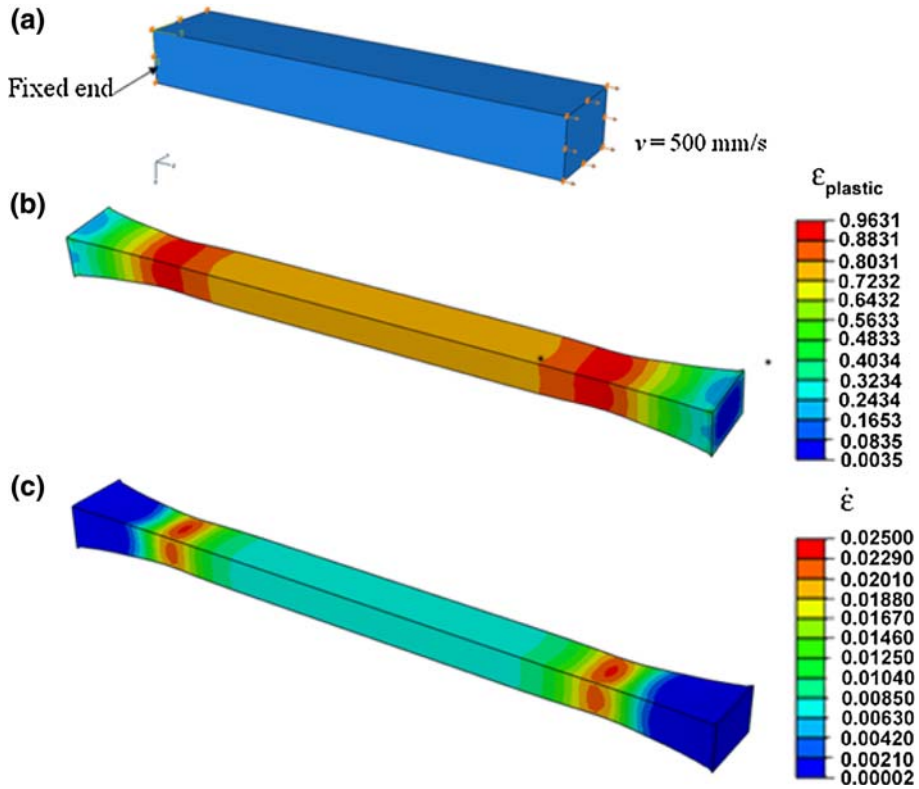

Fig. 10. Finite element analysis of a 32-mm-long bar subjected to 500 mm/s velocity load: (a) boundary conditions, (b) contour plot of the maximal principal plastic strain at t = 56 ms, where the double necking is clearly observed, consistent with experiments, and (c) contour plot of the maximal principal strain rate at t = 56 ms.

The following two criteria were used to simulate the necking: (1) local maximal principal plastic strain exceeding 50%, or (2) local maximal principal strain rate larger than 10/s. These are relatively arbitrary criteria; experimental measurements are being conducted to obtain more accurate values of

the local plastic strain and strain rate. The rate-dependent stress–strain relation was based on Long et al.'s[25] experiments, with a Young's modulus of 46 GPa, Poisson's ratio of 0.3, and density of 7.6 g/cm^3. Our experimental measurements show that both the strain and displacement in the fillet region are relatively small compared with the strain in the gage section. Thus, a three-dimensional (3D) rectangular model representing the gage section only was used in the simulations.

Figure 10a shows results of the simulation of the ASTM specimen. A velocity of 500 mm/s was imposed at one end while keeping the other end fixed. The contour plot of the maximum principal plastic strain on the deformed bar, at t = 56 ms, clearly shows double necking near the free and fixed ends. Figure 10b shows that the majority of the specimen has reached 50% plastic strain, so plastic strain alone cannot explain the double-necking phenomenon. This is reasonable since under low strain rates under uniaxial tension, double necking does not take place. Figure 10c shows the contour of the maximal principal strain rate at the same time, t = 56 ms. Here, the localized strain rate reaches the necking criterion (10/s) only at the two double-necking sites near the two ends. Since the maximal localized strain rate only appears at the double-necking sites, it appears that the localized strain rate is a better indicator than plastic strain in terms of where necking will take place.

In addition to specimen geometry, the effect of strain rate was also investigated. A series of simulations were conducted at varying displacement rates, from 100 mm/s to 400 mm/s. Table III summarizes the relationship between double necking and maximal principal plastic strain and localized strain rate. It is interesting to note that double necking only takes place above a critical strain rate of about 10/s, which correlates well with our experimental results. Based on these data we conclude that the local plastic strain rate, closely related to the displacement rate, plays an important role in the potential sites for necking.

Table III. Relationship Between Double-Necking with Maximal Plastic Strain and Localized Strain Rate for a 32 mm Long Bar

Velocity (mm/s)	Maximal Principal Plastic Strain (%)	Maximal Localized Strain Rate (/s)	Double Necking	Time When Necking First Visible (ms)
100	50.7	2.8	No	170
200	51.6	6.0	No	92.5
300	57.1	10.3	Yes	67.5
400	57.8	11.1	Yes	53.1
500	55.6	12.8	Yes	41.4

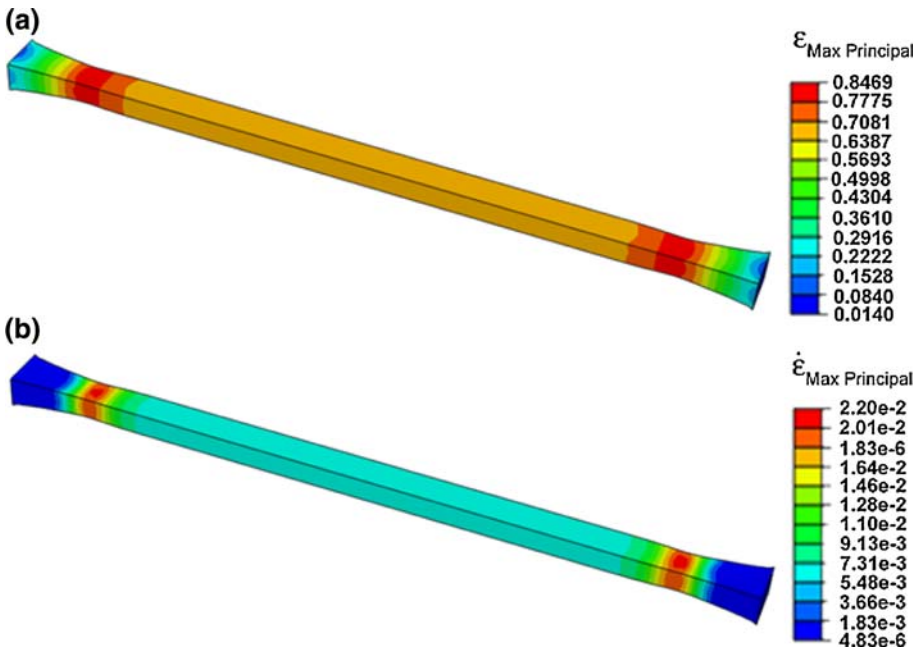

Fig. 11. Finite element analysis of a 50-mm-long bar subject to 700 mm/s velocity load: (a) contour plot of the maximal principal plastic strain at t = 70 ms, where double necking is observed, and (b) contour plot of the maximal principal strain rate at t = 70 ms.

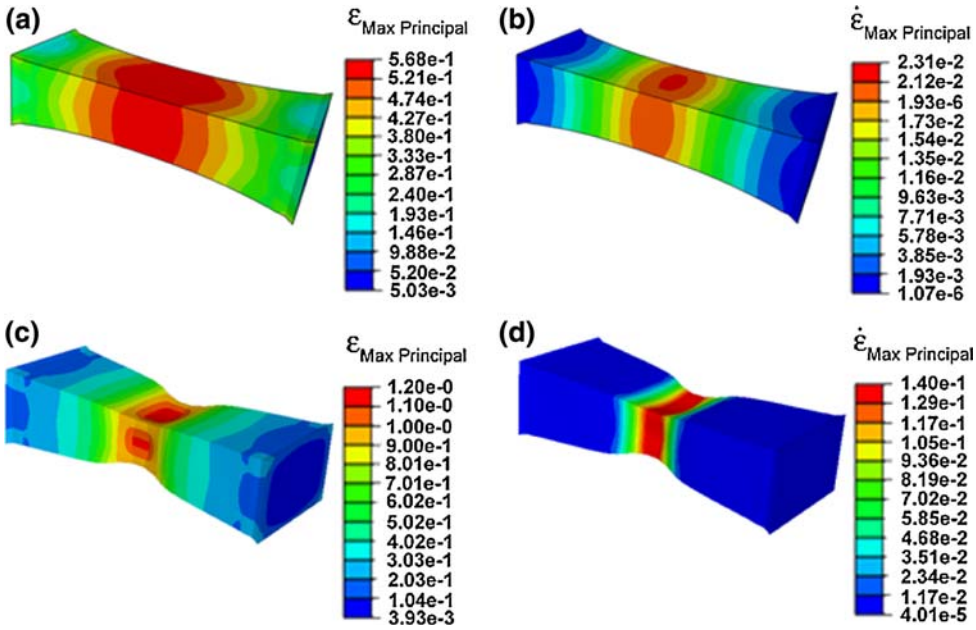

Fig. 12. Finite element analysis of a 10-mm-long bar subject to 150 mm/s velocity load: (a) contour plot of the maximal principal plastic strain at $t = 35$ ms, where necking is not observed, (b) contour plot of the maximal principal strain rate at $t = 35$ ms, (c) contour plot of the maximal principal plastic strain at $t = 45$ ms, where single necking is observed, and (d) contour plot of the maximal principal strain rate at $t = 45$ ms.

We also varied the length of the gage section to study the effect of geometry on necking. Figure 11 shows double necking at $t = 70$ ms in a 50-mm-long bar subjected to a displacement rate of 700 mm/s. Once again, the maximal principal plastic strain reaches the necking criterion globally throughout the gage section (Fig. 11a), while the maximal principal strain rate criterion is met locally, as in Fig. 11b. The same results were observed in the case of the 32 mm gage section (Fig. 10 and Table III). For a bar with a shorter gage section, i.e., $L = 10$ mm, subjected to 150 mm/s velocity load, double necking was not observed (Fig. 12). Because of the shorter gage section, the maximal principal strain rate is not localized at either of the two sites for potential double necking (Fig. 12b). Eventually, at time $t = 45$ ms, single necking takes place (Fig. 12c and d). These two simulations show that the length of the gage section also plays an important role. Double necking only occurs for the specimens with relatively long gage sections. The critical length of the gage section may also depend on various parameters, such as constitutive behavior of the material and displacement rate.

CONCLUSIONS

We have conducted a preliminary study on the intermediate strain rate behavior of pure Sn solder. The following conclusions can be drawn:

1. FEM analysis showed that a modified specimen geometry, with a 10 mm gage length, provided a homogeneous strain distribution, similar to that for the ASTM-E8 specimen geometry. The smaller gage length enabled us to obtain a higher strain rate for a given applied displacement rate.
2. Ultimate tensile strength and strain to failure in the 10 mm specimen were quite similar to those of the ASTM specimen. A double-necking phenomenon was observed in the ASTM specimen, which was not observed in the 10 mm specimen. It would appear that the 10 mm specimen is more suitable for obtaining reliable and accurate constitutive data for FEM reliability models.
3. High-speed video coupled with fiducial markings on the specimen surface was used to correlate the local deformation mechanisms with the measured stress–strain behavior. This technique is quite valuable in trying to understand the behavior of solder alloys at intermediate strain rates.
4. FEM modeling of the dynamic behavior of the solder correlated very well with the experimental observations. In particular the trends observed in experiments could be rationalized based on the FEM modeling results.

ACKNOWLEDGEMENTS

The authors are grateful for financial support for this work from the National Science Foundation, Division of Materials Research—Metals Division (Drs. Alan Ardell, Bruce MacDonald, and Harsh Chopra, Program Directors).

REFERENCES

1. N. Chawla, *Int. Mater. Rev.* (2009) in press.
2. J. Glazer, *Int. Mater. Rev.* 40, 65 (1995).
3. J. Glazer, *J. Electron. Mater.* 23, 693 (1994).

4. Lead-Free Solder Project. *National Center for Manufacturing Sciences*, August 1997.
5. M. McCormack and S. Jin, *JOM* 45, 36 (1993).
6. P.T. Vianco and D.R. Frear, *JOM* 7, 14 (1993).
7. W.J. Plumbridge, *J. Mater. Sci.* 3, 2501 (1996).
8. R.S. Sidhu and N. Chawla, *Metall. Mater. Trans.* 39A, 799 (2008).
9. R.S. Sidhu and N. Chawla, *Metall. Mater. Trans.* 39A, 340 (2008).
10. R.S. Sidhu, X. Deng, and N. Chawla, *Metall. Mater. Trans.* 39A, 349 (2008).
11. M. Kerr and N. Chawla, *Acta Mater.* 52, 4527 (2004).
12. J.E. Field, S.M. Walley, W.G. Proud, H.T. Goldrein, and C.R. Siviour, *Int. J. Impact Eng.* 30, 725 (2004).
13. T.Y. Tee, H.S. Ng, C.T. Lim, E. Pek, and Z. Zhong, *Microelectron. Reliab.* 44, 1131 (2004).
14. D. Reiff and E. Bradley, *2005 Electronic Components and Technology Conference* (2005) pp. 1519–1525.
15. M. Date, T. Shoji, M. Fujiyoshi, K. Sato, and K.N. Tu, *IEEE 2004 Electronic Components and Technology Conference* (2004), pp. 668–674.
16. K.T. Tsai, F.-L. Liu, E.H. Wong, and R. Rajoo, *Solder. Surf. Mt. Technol.* 18, 12 (2006).
17. R. Pandher and M. Boureghda, *IEEE 07CH37867 45th Annual International Reliability Physics Symposium* (Phoenix, 2007), pp. 107–112.
18. K. Newman, *Proceedings of the 55th Electronic Components & Technology Conference*, June (Orlando, FL, 2005), pp. 1194–1200.
19. J.Y.H. Chia, B. Cotterell, and T.C. Chai, *Mater. Sci. Eng. A* 417, 259 (2006).
20. B.L. Boyce and T.B. Crenshaw, SAND2005-5678 (2005).
21. D.E. Grady and D.A. Benson, *Exp. Mech.* 12, 393 (1983).
22. V.B. Shenoy and L.B. Freund, *J. Mech. Phys. Solids* 47, 2209 (1999).
23. P.R. Guduru and L.B. Freund, *Int. J. Solids Struct.* 39, 5615 (2002).
24. ABAQUS Inc., *ABAQUS Analysis User's Manual V. 6.7* (2007).
25. X. Long, I. Dutta, V. Sarihan, and D.R. Frear, *J. Electron. Mater.* 37, 189 (2008).